Received: 29 March 2024 | Accepted: 29 August 2024

DOI: 10.1111/ejn.16538

RESEARCH REPORT

EJN European Journal of Neuroscience FENS WILEY

Synaptic integration of somatosensory and motor cortical inputs onto spiny projection neurons of mice caudoputamen

Vandana Sampathkumar[1,2] | **Kevin P. Koster**[1] | **Briana J. Carroll**[1] | **S. Murray Sherman**[1] | **Narayanan Kasthuri**[1,2]

[1]Department of Neurobiology, University of Chicago, Chicago, IL, USA

[2]Biosciences Division, Argonne National Laboratory, Lemont, IL, USA

Correspondence
S. Murray Sherman, Department of Neurobiology, University of Chicago, Chicago, IL 60637, USA.
Email: msherman@bsd.uchicago.edu

Funding information
This work was supported by NIH Grant Nos. NS094184 and NS113922 and a NSF Neuronex 2014862.

Edited by: John Foxe

Abstract

The basal ganglia play pivotal roles in motor control and cognitive functioning. These nuclei are embedded in an anatomical loop: cortex to basal ganglia to thalamus back to cortex. We focus here on an essential synapse for descending control, from cortical layer 5 (L5) onto the GABAergic spiny projection neurons (SPNs) of the caudoputamen (CP). We employed genetic labeling to distinguish L5 neurons from somatosensory (S1) and motor (M1) cortices in large volume serial electron microscopy and electrophysiology datasets to better detail these inputs. First, M1 and S1 synapses showed a strong preference to innervate the spines of SPNs and rarely contacted aspiny cells, which are likely to be interneurons. Second, L5 inputs commonly converge from both areas onto single SPNs. Third, compared to unlabeled terminals in CP, those labeled from M1 and S1 show ultrastructural hallmarks of strong driver synapses: They innervate larger spines that were more likely to contain a spine apparatus, more often had embedded mitochondria, and more often contacted multiple targets. Finally, these inputs also demonstrated driver-like functional properties: SPNs responded to optogenetic activation from S1 and M1 with large EPSP/Cs that depressed and were dependent on ionotropic but not metabotropic receptors. Together, our findings suggest that individual SPNs integrate driver input from multiple cortical areas with implications for how the basal ganglia relay cortical input to provide inhibitory innervation of motor thalamus.

KEYWORDS
basal ganglia, cortical layer 5, driver

Abbreviations: APX, engineered ascorbate peroxidase; APX-C/M, APX labeling of cytoplasm/mitochondria; DAB, diaminobenzidine; CP, caudoputamen; EM, electron microscopy; EPSP/C, excitatory postsynaptic potential/current; L5, layer 5 of cortex; M1 or S1, primary motor or sensory cortex; SPN, spiny projection neuron.

1 | INTRODUCTION

The basal ganglia are a collection of interconnected subcortical nuclei responsible for motor learning, motivated

behaviours, habit formation, as well as emotional and cognitive functions (Lanciego et al., 2012). The primary target of external afferents to the basal ganglia, the caudoputamen (CP), is among the largest contiguous structures in the mouse brain (Wilson, 2004). The predominant cell type of the CP, constituting 96–98% of the total cell population by some estimates (Kaiser et al., 2016; Kemp & Powell, 1971), is the spiny projection neuron (SPN). The rest of the CP cells consist of various GABAergic interneurons characterized on the basis of different immunocytochemical properties (Tepper et al., 2018; Wilson, 2004).

Afferents to the CP include the thalamus and dopaminergic inputs from the substantia nigra pars compacta, but by far, the largest input anatomically arises from cortical layer 5 (L5) (Lanciego et al., 2012). Potentially thousands of L5 synapses converge on any single SPN (Wilson, 2013). Accordingly, the CP receives overlapping inputs from the motor and somatosensory cortices (Alloway et al., 2006; Hintiryan et al., 2016; Hoffer & Alloway, 2001), where it presumably integrates sensorimotor information streams. Indeed, functional in vivo experiments show that single SPNs can receive a direct motor cortex input and respond to somatosensory signals driven by whisker deflection (Charpier et al., 2020), suggesting somatosensory and motor cortical inputs may converge onto single cells, and optogenetic evidence supports this convergence (Hooks et al., 2018).

To confirm and extend this evidence for convergence, we genetically labeled long-range axonal projections from the primary motor and somatosensory cortices (M1 and S1) with distinct markers and visualized their terminal zones in CP with large volume serial electron microscopy (EM). Using the same approach, we previously showed that L5 inputs from M1 and S1 converge onto single neurons in the posterior medial thalamus (Sampathkumar et al., 2021a). Furthermore, these L5 corticothalamic inputs are known to have driver properties (Sherman & Guillery, 2013; Usrey & Sherman, 2019, 2021). Given the organization of sensorimotor inputs to CP, we asked whether we might find an analogous convergence of M1 and S1 L5 inputs onto single SPNs and whether the synaptic features might be driver and distinct from other inputs to these cells. We demonstrated this to be the case by using genetic labeling paired with large volume serial EM plus in vitro electrophysiological recordings.

2 | RESULTS

We utilized Rbp4-*cre* transgenic mice, which express *cre* recombinase in cortex effectively limited to cells in L5 (Gerfen et al., 2013; Harris et al., 2014). We delivered two distinct types of Cre-dependent adeno-associated viruses (AAVs) (Figure 1a) with the ascorbate peroxidase (APX) (Martell et al., 2017) targeted either to the cytoplasm (APX-C) or to the mitochondria (APX-M) in S1 and M1 of the same Rbp4-*cre* transgenic mouse. In one mouse, APX-M was delivered to S1 and APX-C to M1 and the labeling was switched in a second mouse (i.e., APX-C was delivered to S1 and APX-M was delivered to M1). We confirmed at the light level discrete regions of diaminobenzidine (DAB) staining at the S1 and M1 injection sites and focused our attention on a lateral region of CP where we predicted M1 and S1 terminals to overlap based on previous anatomical experiments (Prasad et al., 2020) (Figure 1b). Here, we selected a densely labeled region to dissect and image with the EM at low resolution (~20 nm X,Y pixel resolution). Upon examining the processed CP tissue with high resolution EM (~10 nm pixel resolution), we often observed the presence of one or the other distinct label in synaptic terminals in CP (Figure 2), located millimetres away from the labeled cell bodies in their respective cortices. In serial EM datasets of CP, despite their proximity to each other, the APX-C- and APX-M-labeled terminals were easily distinguished from one another as well as from unlabeled terminals.

Table 1 summarizes the data on which this study is based.

2.1 | Convergence of M1 and S1 inputs onto spiny neurons in CP

We have previously demonstrated that S1 and M1 synapses converge onto the same post-synaptic neurons in higher order thalamus, the posterior medial thalamus (Sampathkumar et al., 2021a). Here, we asked whether we could find analogous convergence from those cortical regions onto single CP neurons or whether these target discrete populations (Figure 1a, bottom). To do this, we focused on CP regions with a high density of labeling from M1 and S1 (Figure 1b). Because we found more labeled terminals from M1 (see below), we reasoned that the best approach to detecting convergence would be to start with a labeled S1 synapse on a dendrite and trace that dendrite to look for evidence of an M1 synapse innervating the same neuron. Virtually all the labeled terminals from S1 and M1 synapsed onto spines of SPNs (see below). Thus, we started with the synapse, from unlabeled or labeled axonal boutons, and traced spine necks back to their parent dendrite. An example reconstruction is shown in Figure 3. Notably, our EM volume allowed us to inspect the entirety of spine necks for innervation (Figure 3a–i, see below).

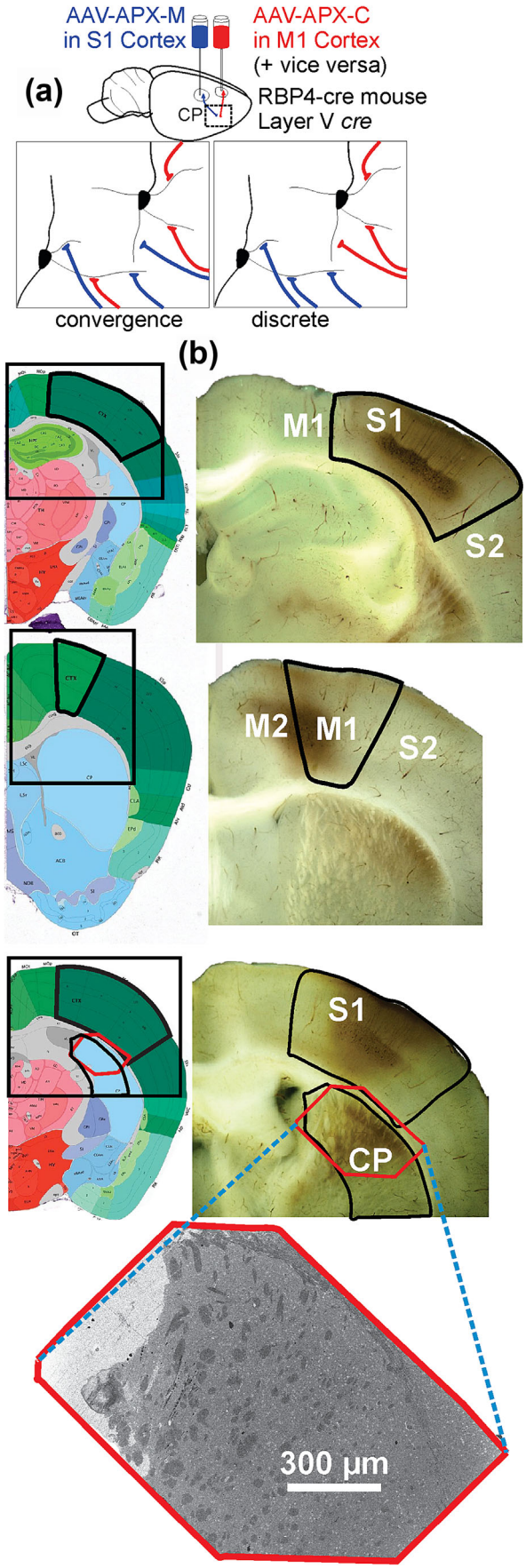

FIGURE 1 Experimental strategy. (a) We administered two types of AAV, APX-C targeting the cytoplasm and APX-M targeting the mitochondria into two Rbp4-*cre* transgenic mice. This approach ensured that labeling in CP was limited to L5 cortical neurons. In one mouse, as depicted, the APX-M virus was injected into S1 cortex and APX-C virus in M1. In the other mouse (not shown), the labeling was reversed with APX-C virus injected into S1 cortex and APX-M virus into M1 cortex. Using this approach, we tested the competing hypotheses that S1 and M1 converged on single SPNs or onto discrete populations of SPNs. (b) DAB reactions on vibratome slices, and corresponding panes from the Allen atlas, show dark staining indicating APX expression limited to L5 cells in injection sites, S1 and M1, as well as the target region, CP. Bottom: low resolution electron micrograph of the dissected CP region. The red boxes and blue dashed lines show where the EM sample was imaged from the image above.

In the first dataset, we traced 21 dendrites/cells and in the second dataset, seven dendrites/cells. Even the most extensive reconstructions did not include the entire dendritic arbor, and in many instances, only a part of a dendrite could be traced before the stack ended. We found evidence of convergence in six SPNs traced in each of the datasets. For three of these six, we located the soma. Examples of traced SPNs from each animal that exhibit convergent S1 and M1 L5 are shown in Figure 4a. Notably, we observed instances where S1 and M1 L5 synapses were closely situated on the same dendrite (10–20 µm apart), while in other cases, the labeled terminals synapsed farther apart on different dendritic branches as illustrated in Figure 4b. Each synapse near the labeled terminals was marked on the dendritic arbor. Numerous unlabeled terminals were observed that also primarily synapsed onto dendritic spines (brown spheres) and, less often, on the shafts (blue spheres) (Figure 4b).

2.2 | S1 and M1 L5 inputs specifically innervate SPNs in CP

We first asked whether L5 axons from S1 and M1 showed a preference for spiny versus aspiny neurons in CP. Our qualitative impression was that the vast majority of labeled terminals in CP from either cortical area synapsed onto spines and thus onto SPNs. To determine if these labeled spine synapses differed on average from unlabeled spine synapses on SPNs, we randomly selected and analysed labeled L5 S1 and M1 synapses in CP, along with annotating every unlabeled terminal within a defined volume ($n = 1465$ labeled; $n = 270$ S1; $n = 1195$ M1; $n = 625$ unlabeled). Unlabeled terminals are a heterogenous population that includes terminals from other afferents to CP as well as unlabeled

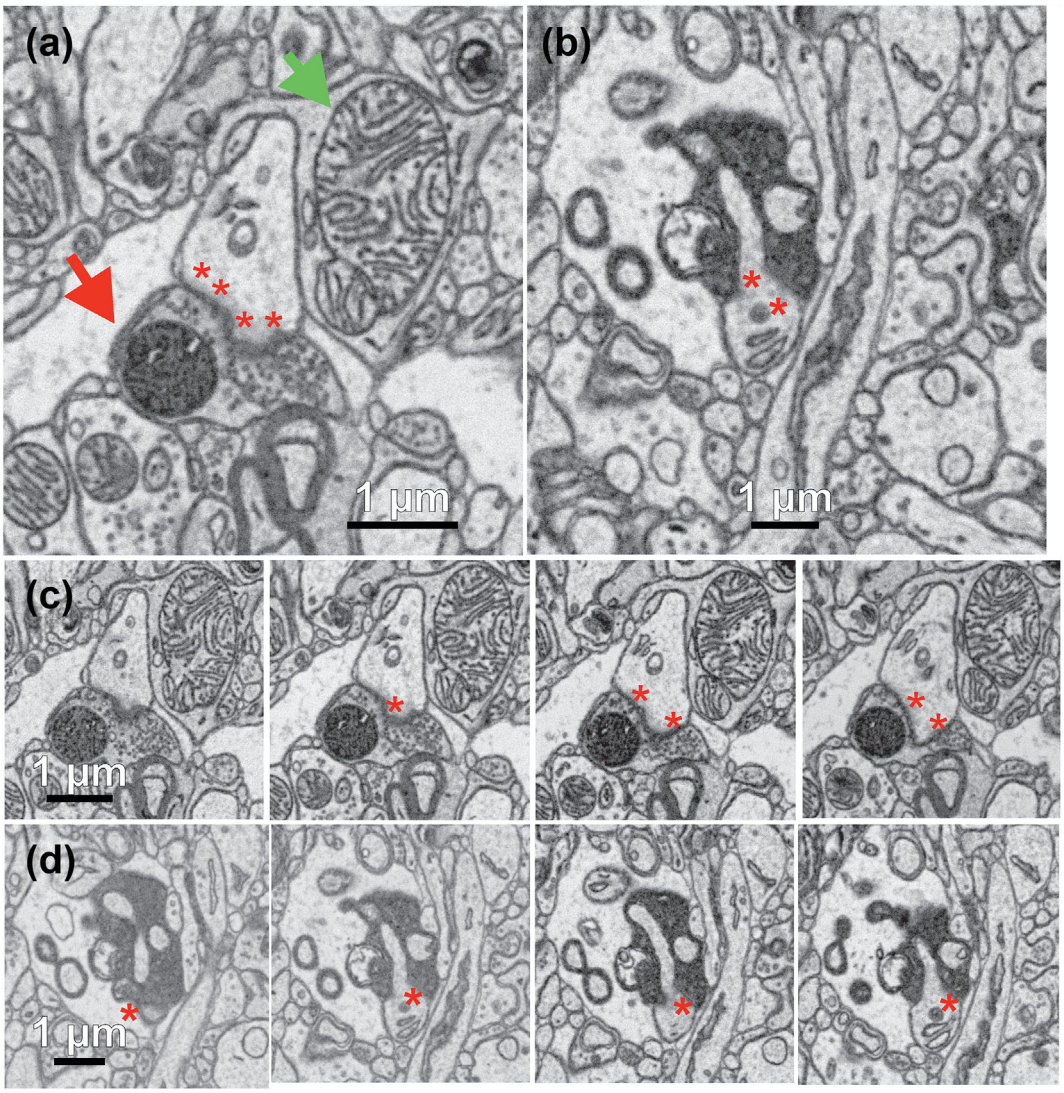

FIGURE 2 Identification of APX-M and APX-C labeled terminals in large volume EM datasets. (a, b) EM micrographs of synapses where the cortical axon has been labeled with either APX-M (a) or APX-C (b). In both cases, synaptic vesicles can be seen in the presynaptic terminal and postsynaptic densities (red asterisks) in dendrites. The red arrow in (a) points to an APX-labeled mitochondrion that is clearly distinguishable from an unlabeled mitochondrion (green arrow). The two bottom rows show a series of EM images through the synapses seen in (a) (row (c)) and (b) (row (d)). Postsynaptic densities are labeled with red asterisks.

L5 terminals (Nauta et al., 1974); we tested whether labeled L5 terminals exhibit properties different on average from this heterogenous sample, suggesting functional specialization relative to other afferents as we have done previously (Sampathkumar et al., 2021b). The unlabeled terminals were annotated in a volume of $15 \times 15 \times 8$ μm^3 and $12 \times 15 \times 8$ μm^3 within the CP regions that had the highest concentration of labeled terminals from S1 and M1 in both datasets. Among the unlabeled terminals annotated, 565 (90.4%) were on spines and 60 (9.6%) were on shafts; 58 of these 60 (96.6%) were on shafts of SPNs, the other two (3.4%) contacting aspiny dendrites. Of the labeled terminals, 1444 (98.6%) synapsed on spines and 21 (1.4%) on shafts; of the latter, nine (0.6%) were on shafts of aspiny neurons, and the other 12 (0.8%) were on the shafts of SPNs. Thus, of the labeled terminals, 1453 (99.2%) synapsed onto SPNs versus nine (0.6%) onto aspiny cells. Relative to unlabeled terminals, the greater prevalence of labeled cortical L5 terminals to synapse onto spines versus shafts is significant ($p = 7.43e{-}26$ on a χ^2 test).

We next asked whether these distributions of innervation patterns reflect the underlying distributions of aspiny and spiny neurons in CP. We reasoned that the total length of SPNs versus aspiny dendrite is a fair measure of the potential target availability for cortical and other afferent inputs. To determine these dendritic lengths, we reconstructed all putative spiny and aspiny

TABLE 1 Quantitative summary of examined spiny neurons and labeled terminals.

Cells studied					
	Traced arbors	**Convergence**	**Traced to Soma**		
Mouse 1	21	6	3		
Mouse 2	7	6	3		
Terminals studied					
	S1	**Spine**	**Shaft**	**Spiny shaft**	**Aspiny shaft**
Mouse 1	127	122	5	4	1
Mouse 2	143	142	5	1	0
	M1	**Spine**	**Shaft**	**Spiny shaft**	**Aspiny shaft**
Mouse 1	277	276	1	0	1
Mouse 2	918	904	14	7	7

Top: In two mice, 28 CP spiny dendritic arbors were identified as postsynaptic targets of terminals from L5 of S1 and/or M1. Of these, convergence of S1 and M1 inputs was seen on 12 CP dendrites, and 6 of these were traced to their parent somas. **Bottom**: In the same two mice, terminals from S1 (upper) and M1 (lower) were further analysed regarding their synaptic locations onto CP spines and shafts, and among the latter, whether the shafts were from spiny or aspiny CP cells.

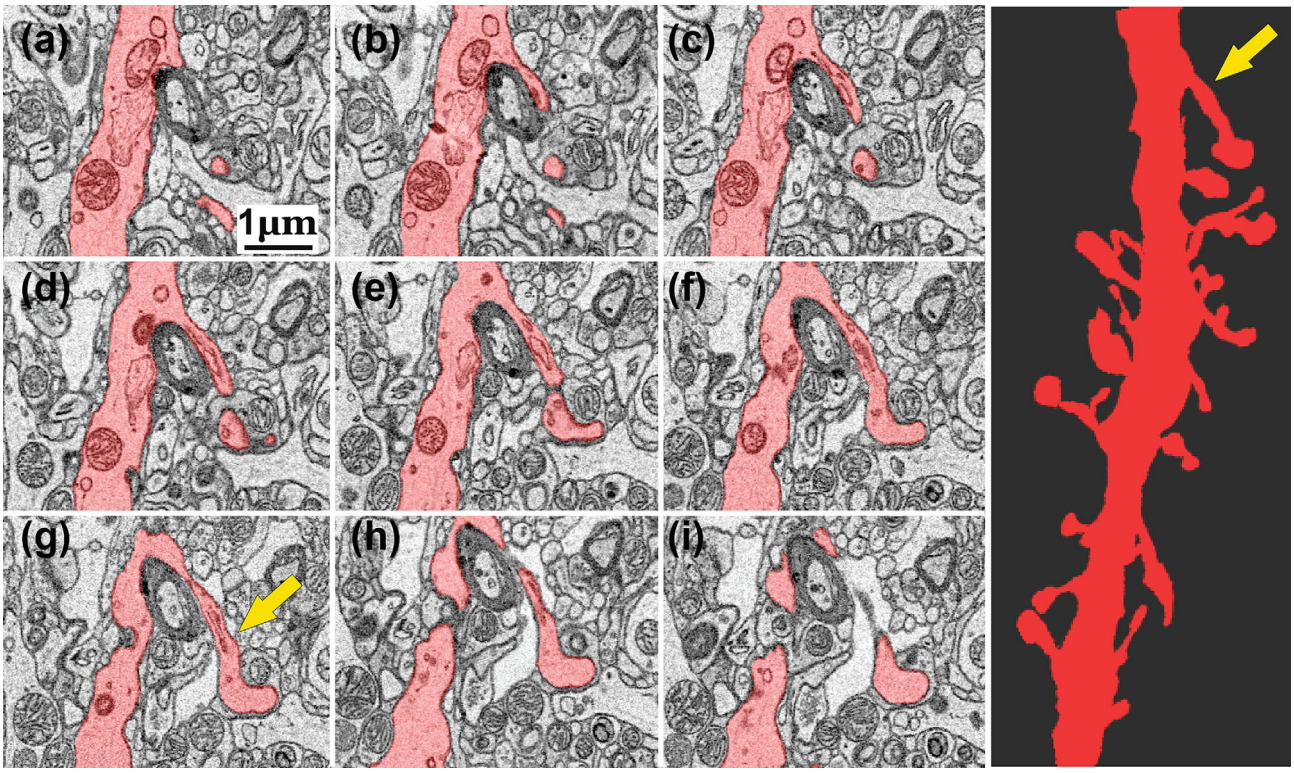

FIGURE 3 Tracing spine necks. (a–i) Serial EM micrographs, 40 nm thick with the spine and spine neck of a spiny dendrite traced in red. (j) A 3D reconstruction of a longer span of the dendrite shown in (a–i). The yellow arrows in (g) and (j) point to the same spine. Spine necks are easily traced in our volumes, and we can clearly identify potential synapses on these necks, and none was found. In the example shown, the spine is singly innervated only at the head by an unlabeled bouton.

dendrites in sub-volumes of our EM datasets, centred on regions where the unlabeled terminals were annotated in the dense overlap zone of labeled S1 and M1 synapses. In volumes from two animals measuring $15 \times 20 \times 15\ \mu m^3$ and $10 \times 20 \times 10\ \mu m^3$, we found 2/54 and 1/26 dendrites were aspiny with a total length of 1443.8 µm of spiny dendrite and 106 µm of aspiny dendrite traced. Given this comparison, unlabeled terminals were more likely than

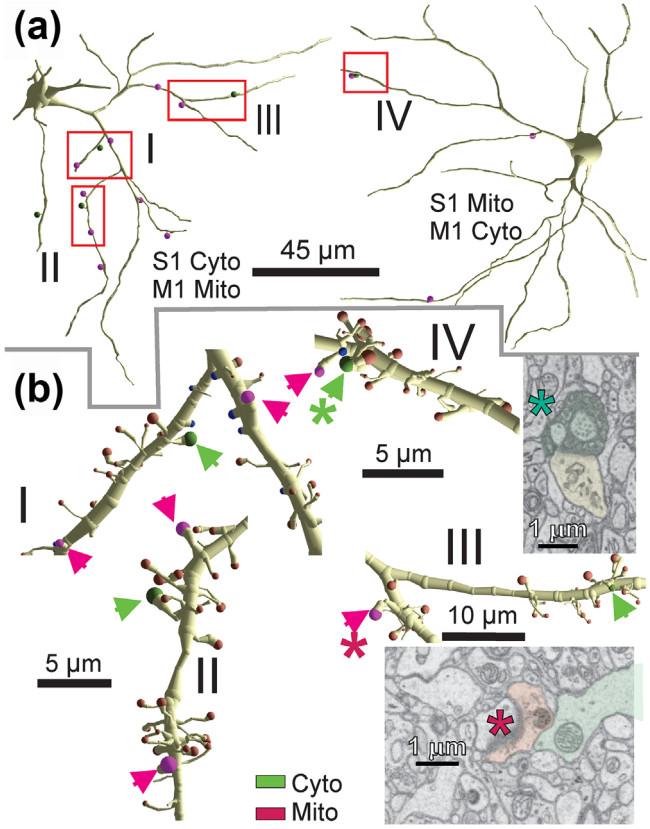

FIGURE 4 Convergence of L5 S1 and M1 inputs onto individual SPNs in CP. (a) In both animals, we observed convergence of synapses originating from L5 S1 and M1 on individual SPNs in CP. Shown are examples of SPNs reconstructed from each animal demonstrating this convergence. Green spheres indicate cytoplasmic labeled terminals, and pink spheres indicate mitochondrial labeled terminals. (b) Detailed reconstructions (labeled as I, II, III and IV) of SPN dendrites shown in (a) These reconstructions encompass all synapses including the labeled and unlabeled ones. The cytoplasmic labeled terminals are depicted as green spheres, mitochondrial terminals as pink spheres, unlabeled terminals on spines as brown spheres and unlabeled terminals on shaft as blue spheres. Representative electron micrographs display the mitochondrial labeled terminal in pink, cytoplasmic labeled terminal in green and the post-synaptic dendrite in yellow; these examples are marked with asterisks in the reconstructions.

chance to target SPNs ($p = 0.028$ on a χ^2 test), and the same was true for labeled L5 terminals ($p = 5.19e{-}19$ on a χ^2 test). Regarding the L5 inputs, there was no significant difference in the innervation patterns of M1- vs S1-labeled terminals ($p = 0.88$ on a χ^2 test). These data indicate that all annotated inputs to CP, labeled and unlabeled, selectively innervate SPNs and avoid aspiny neurons; however, as noted above, both L5-labeled populations have a significantly larger fraction of terminals innervating SPNs than do unlabeled terminals, making these L5 inputs even more selectively target SPNs.

2.3 | Quantitative differences between S1 L5, M1 L5, and unlabeled terminals synapsing onto SPNs in CP

We then analysed whether M1 and S1 L5 synapses in CP were ultrastructurally different from each other and from the broader population of synapses represented by unlabeled terminals. Our analysis focused on six key measurements for comparison: (1) pre-synaptic terminal diameter (Figure 5a), (2) post-synaptic spine diameter (Figure 5b), (3) the presence or absence of a spine apparatus in the postsynaptic spine (Figure 5cf) (Spacek, 1985), (4) the presence or absence of mitochondria in the terminal (Figure 5d), (5) the percentage of terminals with multiple postsynaptic targets (Figure 5e), and (6) post-synaptic dendritic diameter (Figure 5c). Each metric has associated functional implications. Spine and terminal size have a strong, positive linear relationship with the magnitude of synaptic strength (Borczyk et al., 2019; Holler et al., 2021; Meyer et al., 2014). The spine apparatus, which is coiled smooth endoplasmic reticulum found in the spine neck, is correlated with potentiated spines (Deller et al., 2003). Mitochondria within synaptic terminals play vital role in managing energy requirements for synaptic activity, synaptic vesicle recycling, modulating short-term plasticity and establishing stable synaptic connections over time (Cserép et al., 2018). Finally, multisynaptic terminals, where a terminal contacts more than one spine in the same dendrite or contacts spines from different neurons, are associated with long-term potentiation (LTP) and motor learning skills as well as function as synaptic transmission centres across many cells (Jones & Powell, 1969; Lee et al., 2013; Toni et al., 1999); such multi-synaptic terminals have also been associated with driver input (Sherman & Guillery, 2013; Van Horn et al., 2000).

All measurements and analysis were done on the 3D EM reconstructed volumes. We found significant differences between synapses formed by APX-labeled L5 S1 and M1 terminals on SPNs compared to unlabeled terminals. We randomly examined 1114 axonal terminals (221 from S1, 268 from M1 and 625 unlabeled) on SPNs and measured each of the aforementioned parameters. First, compared to unlabeled, labeled terminals were larger and synapsed on larger spines. For terminal diameters (Figure 5a), the comparison is 819.9 ± 13.4 nm (mean ± SE) for S1, 812.8 ± 11.1 nm for M1, and 649.0 ± 7.9 nm for unlabeled. Terminals from S1 and M1 were both significantly larger than unlabeled terminals ($p < 0.0001$ on Mann–Whitney U tests); there was no significant difference in these measures between S1 and M1 terminals. We found a similar pattern for the diameter of heads of postsynaptic spines (Figure 5b):

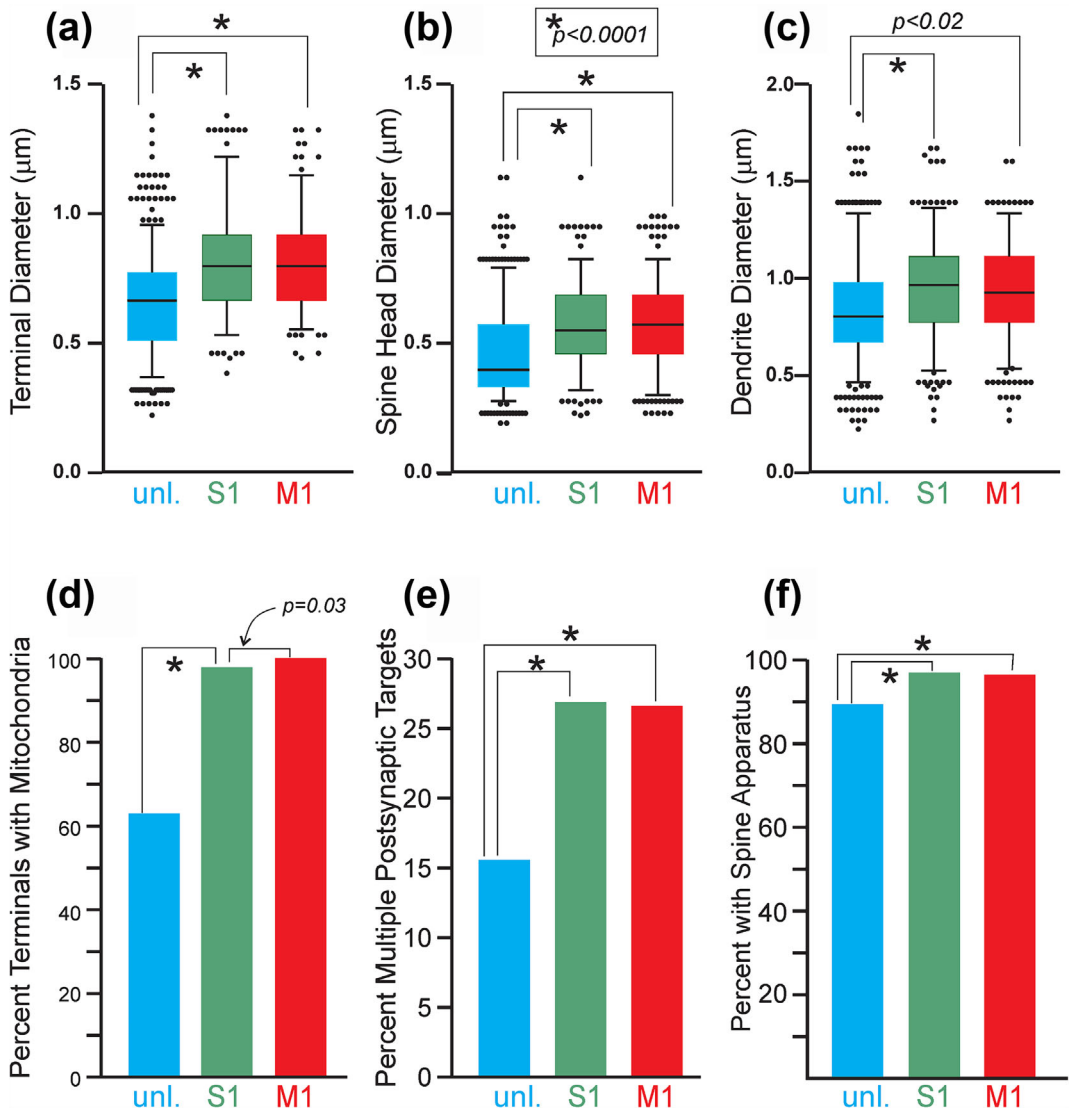

FIGURE 5 Quantitative differences between labeled and unlabeled (unl.) synapses onto SPNs in CP. (a) Terminal diameter. (b) Spine head diameter. (c) Diameter of postsynaptic dendrite. (d) Percentage of presynaptic terminals containing mitochondria. (e) Percentage of multiple postsynaptic targets innervated by each terminal. (f) Percentage of postsynaptic spines with spine apparatus. See text for Values represnted by asterisks.

545.9 ± 9.1 nm (mean ± SE) for S1, 557.7 ± 8.7 nm for M1, and 445.6 ± 6.1 nm for unlabeled. Again, the values for spines targeted by S1 and M1 were both significantly larger than those targeted by unlabeled terminals ($p < 0.0001$ on Mann–Whitney U tests); there was no significant difference in these measures between S1 and M1 terminals.

Regarding the presence of a spine apparatus in the postsynaptic spine (Figure 5c), unlabeled terminals were less likely to innervate such spines (590 out of 668; 88.3%) than either S1 (289 out of 297; 97.3%) or M1 (342 out of 355; 96.3%) ($p < 0.00001$ on χ^2 tests for both comparisons). We found no significant difference in this parameter between M1 and S1 terminals. We also found differences in the likelihood of mitochondria found in terminals (Figure 5d). Of unlabeled terminals, 389 of 624 (62.3%) had at least one mitochondrion, which is a smaller percentage than that for terminals from either S1 (215 of 221; 97.3%) or M1 (267 of 268; 99.6%) ($p < 0.00001$on χ^2 tests for both comparisons). However, more M1 than S1 terminals tended to have a mitochondrion ($p = 0.03$ on a χ^2 test). We also determined how often these terminals formed synapses with more than one post-synaptic target (Figure 5e) as has been described for retinogeniculate synapses (Van Horn et al., 2000). Of 625 unlabeled terminals, 95 (15.2%) contacted multiple targets, which is a lower ratio than for either S1 (59 out of 221; 26.7%) or M1 (71 of 268; 26.5%) ($p < 0.00001$on χ^2 tests) for both comparisons. Again, we found no difference in this parameter between M1 and S1 terminals.

Finally, we measured the dendritic diameters at the base of postsynaptic spines (Figure 5f). These values were significantly different among our samples: 865.4 ± 9.9 nm for unlabeled terminals versus 918.7 ± 14.5 nm for S1 terminals (p =0.0026 on a $\chi 2$ test)and 898.5 ± 13.1 nm for M1 terminals(p =0.0026 on a $\chi 2$ test). The dendrite diameters were larger for labeled when compared to unlabeled terminals. There was no difference between S1 and M1 terminals (p =0. 2981on a $\chi 2$ test).

2.4 | Lack of multiple inputs to spines of SPNs

It has been reported that many spines of SPNs have, in addition to a synapse on the spine head, a second, frequently dopaminergic, one on the spine shaft (Freund et al., 1984; Jones, 2007). Quantitative approaches sampling a limited number (e.g. 46 or 87) of dendritic spines suggest that between 8% and 39% of spines have such an arrangement (Freund et al., 1984; Wilson et al., 1983). We found little evidence of this pattern. Of 27 spines targeted by M1 L5 afferents, none had a second input, and of 26 targeted by S1 L5 afferents, one had a second input. Furthermore, of 50 spines targeted by unlabeled terminals, none had a clear second input.

2.5 | Relationships among morphological parameters

We found that, among all terminal classes, terminal diameter correlated with the diameter of the spine head: for M1 terminals, $r = 0.27$, $p = 0.0012$; for S1 terminals, $r = 0.34$, $p = 0.00007$; and for unlabeled terminals, $r = 0.36$, $p < 0.00001$. For S1 and M1 terminals, none of the other correlations (i.e. terminal vs dendritic diameter or spine head vs dendritic diameter) was statistically significant ($p > 0.05$ for each). However, for unlabeled terminals, spine and dendrite diameters correlated ($r = 0.211$, $p = 0.002$).

2.6 | S1 and M1 L5 inputs to CP spiny projection neurons are drivers

Our analyses above suggest that S1 and M1 synapses in CP showed many of the ultrastructural characteristics of driver synapses (Sherman & Guillery, 1998, 2013), and since L5 corticothalamic projections tested have proven uniformly to be drivers (Miller-Hansen & Sherman, 2022; Mo & Sherman, 2019), we next asked whether S1 and M1 L5 inputs to CP showed driver properties, namely depressing synaptic responses activated exclusively via ionotropic glutamate receptors (iGluRs) and with no metabotropic receptor (mGluR) contribution. A recent study tested the synaptic properties of S1 and M1 to CP in a similar manner (Johansson & Silberberg, 2020; Lee et al., 2019; Morgenstern et al., 2022) but optogenetically activated these inputs via terminal stimulation, which is known to produce artefactual paired-pulse effects (Jackman et al., 2014; Miller-Hansen & Sherman, 2022; Mo & Sherman, 2019). Therefore, we tested the synaptic properties of these inputs to the CP by photostimulation of S1 or M1 L5 ChR2-postive axons at sites >300 μm from the recorded cell body.

First, in an anatomical experiment, we used fluorescence microscopy of brains from Rbp4-*cre* mice injected with two separate, Cre-dependent anterograde labels, and this revealed the dorsal portion of the CP between −0.4 and −0.8 mm posterior from bregma to contain robust overlap between S1 and M1 L5 terminal fields (Figure 6a), consistent with other published data (Lee et al., 2019; Oh et al., 2014). We thus localized our in vitro recordings to this overlap region. We physiologically identified SPNs by their hyperpolarized resting membrane potential, low input resistance and latency to fire in response to direct current injection (i.e. in contrast to local interneurons which exhibit distinct physiological features) (Kreitzer, 2009). We then evoked EPSCs in these neurons by focal laser stimulation of descending S1 or M1 L5 axons (driven by Cre-dependent expression of ChR2 in Rbp4-*Cre* mice) in the cortical white matter as described above (Figure 6b). Trains of laser-stimulated EPSCs (1 ms pulses, 10 Hz) demonstrated a depressing paired-pulse phenotype of both S1 (Figure 6ci) and M1 (Figure 6cii) L5 inputs. Analysing the paired-pule ratio for all cells with a ChR2-dependent response (seven cells from four mice for S1 L5, seven cells from three mice for M1 L5) and activation of iGluRs but not mGluRs (four cells from two mice tested for M1 L5 inputs and two cells from two mice tested for S1 L5 inputs) consistently showed that L5 inputs to SPNs in the CP are drivers (Figure 6c). The amplitudes of the first laser evoked EPSCs for M1 L5 inputs to CP neurons were greater than those elicited by L5 S1 axon stimulation (Figure 6d), but the difference does not quite reach statistical significance ($p = 0.055$ on a Mann–Whitney U test).

3 | DISCUSSION

We utilized automated serial EM and genetic labeling to investigate the long-range connections from L5 of S1 and M1 to the CP region of the basal ganglia. As has been reported, we found that S1 and M1 terminals overlap in CP (Hintiryan et al., 2016; Hoffer & Alloway, 2001; Hooks et al., 2018; Prasad et al., 2020; Smith et al., 2022),

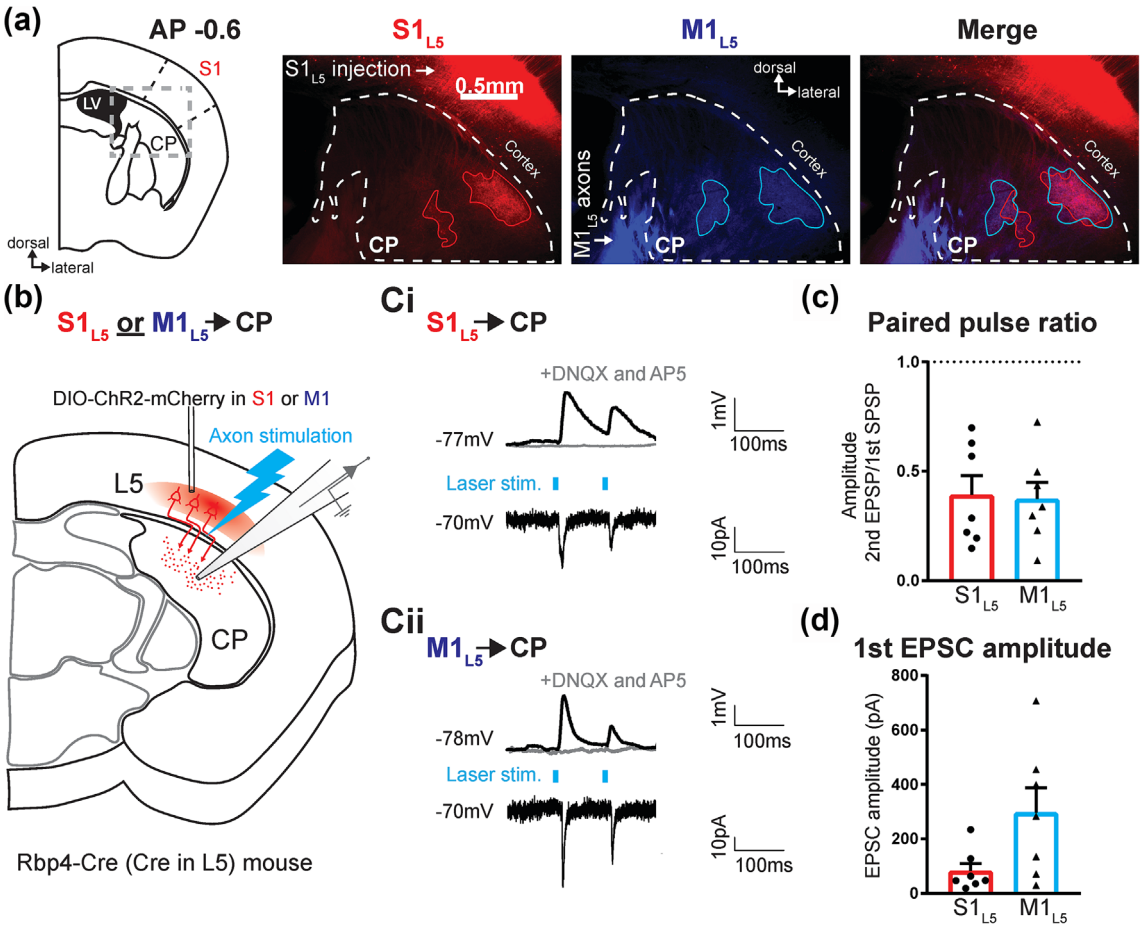

FIGURE 6 L5 S1 and M1 projections to CP act as drivers. (a) Representative images of dual-anterograde labeling of $S1_{L5}$ (red) and $M1_{L5}$ (blue) in the same mouse, demonstrating distinct but partially overlapping terminal fields in CP at −0.6 mm posterior from bregma. LV, lateral ventricle. Colour-coded annotations represent the outer bounds of their respective terminal fields in CP. (b) Schematic of the physiology experiment, in which L5 of either S1 or M1 was transduced with ChR2 and laser-stimulated evoked responses elicited at axons (>300 μm from recorded cell, lighting bolt symbol) were recorded postsynaptically in CP neurons. (ci) Current clamp (top) and voltage clamp (bottom) whole-cell recordings demonstrating that 10 Hz laser stimulation (light blue squares) of the $S1_{L5}$ inputs to CP neurons is depressing (2 pulses shown for simplicity), and that application of DNQX (50 μM) and AP5 (100 μM) completely abolishes all laser-induced excitation. (cii) Current clamp (top) and voltage clamp (bottom) whole-cell recordings demonstrating that 10 Hz laser stimulation (light blue squares) of the $M1_{L5}$ inputs to CP neurons is depressing (two pulses shown for simplicity), and that application of DNQX (50 μM) and AP5 (100 μM) completely abolishes all laser-induced excitation. (d) Summary paired-pulse ratio data (second EPSP amplitude/first EPSP amplitude) demonstrating that all CP neurons recorded receive an $M1_{L5}$ or $S1_{L5}$ input that has driver-type synaptic properties (paired-pulse ratio < 1.0; $n = 7$/group). (e) Amplitudes of first EPSC evoked by photostimulation of $S1_{L5}$ or $M1_{L5}$ axons while holding the cell at −70 mV (voltage clamp). $p = 0.055$ by Mann–Whitney U test.

but we further show that often these terminals converge to innervate the same SPN. We compared these L5 terminals to wider population of unlabeled terminals in the same region and found several significant differences on average: Compared to unlabeled terminals, those from L5 were larger, contacted larger spines that more often had spine apparatuses, more often included mitochondria, and more often made contacts onto multiple postsynaptic targets. The only difference found between S1 and M1 L5 terminals was a tendency for the latter to more often produce terminals with mitochondria. Curiously, we found that both labeled and unlabeled terminals selectively contacted spines and SPNs: 99.6% of unlabeled and 99.4% of labeled terminals targeted SPNs, leaving rather little input to aspiny neurons in CP. This targeting appears selective, because the percentage of terminals of both types targeting SPNs is greater than the ratio of available SPN versus aspiny dendrite in the region.

3.1 | Technical limitations

There are several potential limitations to our approach. First, we did not label all L5 cortical neurons contributing to M1 and S1 pathways under study here, since it appears that not all L5 cells in Rbp4 mice contain

Cre-recombinase (Harris et al., 2014), and many other cortical areas also innervate CP (reviewed in Lanciego et al. (2012)). These other cortical inputs contribute to the population of unlabeled cortical terminals in our study, and thus, the differences we found between labeled and unlabeled terminals almost certainly underestimate the difference between cortical L5 and other inputs to CP. Furthermore, we cannot exclude the possibility that the Rbp4-*cre* line is selective for a particular class of L5 neurons in both M1 and S1, and unlabeled L5 neurons from S1 and M1 might exhibit properties different from those reported here. Nonetheless, the significant differences we document between labeled and unlabeled terminals suggest that the distinctions we highlight here are robust. Second, because we could not identify many L5 inputs from cortex and because we did not reconstruct the entire dendritic arbors of SPNs, it is likely that we have underestimated the convergence of L5 inputs from different cortical areas onto SPNs.

3.2 | L5 S1 and M1 synapses are driver inputs onto SPNs

Our morphological analysis of L5 afferents to CP, including terminal size plus presence of mitochondria, postsynaptic spine features, and multiple targets for many terminals, indicates driver synapses (Borczyk et al., 2019; Cserép et al., 2018; Deller et al., 2003; Holler et al., 2021; Meyer et al., 2014; Sherman & Guillery, 2013; Van Horn et al., 2000). Our electrophysiological results extend these findings by demonstrating that these L5 inputs to CP cells also exhibit physiological characteristics of drivers.

3.3 | Convergence of cortical L5 inputs

We had previously demonstrated that S1 and M1 L5 inputs converge onto excitatory projection neurons in higher order thalamus (Sampathkumar et al., 2021a), and here, we show this pattern of convergence extends to inhibitory cells (e.g. GABAergic SPNs) in the caudoputamen, which is consistent with electrophysiological observations made in vivo (Charpier et al., 2020). It is also noteworthy that these examples of convergence in CP and thalamus involve driver inputs, suggesting integration of information in these circuits.

3.4 | Inputs to spines of SPNs rarely involved multiple synapses

The organization of dopaminergic inputs to SPNs is the subject of intense study reflecting the behavioural and pathological consequences of altered dopamine signaling. It has been claimed that dopaminergic inputs to CP often target SPNs on the necks of spines that receive cortical excitatory inputs (Jones, 2007) and that nearly 40% of dendritic spines in CP contain a second, dopaminergic synapse (Freund et al., 1984), although the authors recognize the potential for an overestimation in their quantitation, which analysed SPNs known to receive dopaminergic inputs. Accordingly, other analyses in rats claimed that only 8%–9% of dendritic spines receive a second synapse (Ingham et al., 1998; Wilson et al., 1983), and only ∼20% of those will be dopaminergic (Wilson, 2004). Our analysis in mice revealed that the number of spines in CP receiving a second synapse from any source is far less than even the lower estimates: only one spine out of 103 analysed, or <1%, had a clear second synaptic input.

Though we are absent a comprehensive explanation that reconciles these data, we offer a few reasons for the quantitative discrepancy. First, we examined SPNs in the dorsolateral CP, while previous studies (i.e. Freund et al., 1984) examined SPNs in the ventral CP, which is more closely tied to reward processing and limbic circuitry (Hunnicutt et al., 2014). Therefore, it is plausible that regional differences in the degree of dopaminergic input to dendritic spines reflect a functional specificity of CP domains, and, accordingly, our estimates reveal a genuine relative sparsity of dopaminergic inputs to SPNs involved in sensorimotor functions of the CP. On the other hand, the study from Freund and colleagues highlights that many of the second synapses onto dendritic spines are composed of tiny, symmetrical active zones formed by en passant fibres that are much less developed than other synaptic contacts. Thus, technical aspects surrounding what constitutes a synapse may have led to an overestimate in the case of Freund et al. (1984), an underestimate in our case, or both, and thus, the actual number of spines with multiple inputs is somewhere between our reports and akin to what was observed by Wilson et al. (1983). Finally, it is plausible that the discrepancy reflects species differences (the cited references were mostly done on rats). Clearly, this detail merits further study.

3.5 | CP targets of S1 and M1 L5 inputs

A remarkable finding is that virtually all terminals we annotated, labeled and unlabeled, target SPNs, with surprisingly little input to aspiny CP cells. A previous anatomical study claims major input from S1 onto parvalbumin-containing aspiny CP cells (Ramanathan et al., 2002), which seems to be at odds with our findings. We have no clear explanation for this and suggest more data are needed to resolve this apparent discrepancy.

3.6 | Comparison of labeled L5 terminals with unlabeled terminals

The differences we note between labeled and unlabeled terminals indicate that the labeled L5 terminals represent a relatively distinct population that is different from most terminals, which are represented by the unlabeled sample. The L5 terminals are, on average, larger, more likely to innervate spines (which are larger), and they innervate larger dendrites suggesting more proximal innervation. All of these features are consistent with the L5 population providing driver input (see Figure 6). These features are also seen in L5 innervation of thalamus (Sherman & Guillery, 2013; Usrey & Sherman, 2019, 2021).

3.7 | Conclusions

Our results emphasize the importance of cortical L5 inputs to the basal ganglia. We find that not only are these inputs numerically dominant, but they also functionally act as drivers. They nearly exclusively target SPNs in CP, largely avoiding aspiny interneurons, and therefore seem to be the major driving force for controlling the outputs of the basal ganglia, particularly the internal segment of the globus pallidus and substantia nigra pars reticulata (Wilson, 2004). These outputs, in turn, provide inhibitory (GABAergic) input to motor thalamus (Wilson, 2004). Thus, these L5 inputs appear to largely control how the basal ganglia gate and modulate these thalamic relays. Finally, we also show that this cortical control of SPNs often involve convergent input from different cortical areas, suggesting that cortical control of basal ganglia may commonly involve the participation of different areas working in concert.

4 | METHODS

4.1 | Animals

All protocols were approved by the University of Chicago Institutional Animal Care and Use Committee. Transgenic mice were bred by crossing female C57BL6J mice with male Tg (Rbp4-Cre) KL100GSat/Mmcd mice (GENSAT RP24-285K21), back-crossed with C57BL/6 mice and maintained in a vivarium (conditions: 12-h light/dark cycle with food and water available ad libitum) (Gerfen et al., 2013). To identify Rbp4-*cre*–positive offspring, tail biopsies were genotyped by Transnetyx prior to performing stereotaxic, Cre-inducible DIO-AAV injections under aseptic conditions.

4.2 | Stereotaxic surgery for electron microscopy

Two Rbp4-*cre* mice (male; 31 and 149 days old) were used in these experiments. Mice were deeply anesthetized using isoflurane, monitored throughout surgery with toe pinches to ensure depth of anaesthesia was maintained and head-fixed in a Kopf stereotaxic frame using bite and ear bars. The scalp was retracted, and a hand drill was used to clear burr holes for two targeted regions in somatosensory cortex (from bregma medial–lateral: 3.1 mm, anterior–posterior: −0.9 mm) and motor cortex (medial–lateral: 2 mm, anterior–posterior: +1.54) (Paxinos & Franklin, 2008). A 1-μL Hamilton syringe (catalogue #14–824-20, Thermo Fisher Scientific) was lowered 0.5 mm below the cortical surface to inject 0.5–1 μL at 60 nL per minute of a virus expressing the enhanced ascorbate peroxidase APX 2.0 in a Cre-dependent fashion (Martell et al., 2017).

Two versions of this virus were used to differentially target the somatosensory and motor cortices: one targeting APX to the cytoplasm (APX-C) and the other to mitochondria (APX-M) (Sampathkumar et al., 2021a). AAV-CAG_DIO-APX2NES (APX-C) was a gift from Joshua Sanes, Harvard University, Cambridge, MA (Addgene plasmid no. 79907; http://www.addgene.org/79907; RRID:Addgene_79907). AAV-CAG-DIO-APEX2Mito (APX-M) was constructed in our laboratory as described previously (Sampathkumar et al., 2021a).

One transgenic mouse was injected with AAV-APX-C and AAV-APX-M in M1 and S1, respectively, and we reversed the injections in a second Rbp4-*cre* mouse to place AAV-APX-C and AAV-APX-M in S1 and M1, respectively.

The syringe was slowly withdrawn, and the scalp incision was sutured closed. An antibiotic (Neosporin) and anaesthetic (lidocaine hydrochloride) were topically applied to the sutures. The analgesic meloxicam was delivered subcutaneously (1 to 2 mg/kg dose) postoperatively and once every 24 h over 2 days. All mice were returned to their cages for a survival period of 27–28 days to allow for transgene expression and transport of the label and then processed for peroxidase staining and large volume EM reconstruction as described below (Sampathkumar et al., 2021a).

4.3 | Electron microscopy

Pentobarbital (60 mg/kg intraperitoneal) was used to deeply anesthetize mice to be nonresponsive to toe pinch and transcardially perfused with 10 mL 0.1 M cacodylate buffer followed by 20 mL of fixative solution composed of

2% paraformaldehyde and 2.5% glutaraldehyde in 0.1 M cacodylate buffer. Each brain was extracted, and either Agmon-Connor's or coronal sections (350 μm thick) were cut using a vibratome. The slices were post-fixed in fixative solution overnight. The sections were then stained with DAB and H_2O_2 to visualize APX labeling (Lam et al., 2015). Briefly, the sections were incubated in 0.5 mg/mL of DAB diluted in 0.1 M cacodylate buffer for 1 h at room temperature. This was followed by treatment with a freshly prepared solution of 0.5 mg/mL of DAB in 0.1 M cacodylate buffer with 1 mM H_2O_2 for 30 min at room temperature. The samples were evaluated at the macro scale for the intensity of the DAB reaction and its localization to S1, M1 and CP. We inspected to confirm that stain through cortex was non-continuous, but rather for distinct stains at our two injection sites, with unstained cortex between these. For CP, we targeted dissections to a lateral region expected to be targeted by both cortical regions based on our previous anatomical investigations (Prasad et al., 2020). The tissues were reduced with 50 mM sodium hydrosulfite in a 60% 0.1 M sodium bicarbonate/40% sodium carbonate buffer for 20 min at room temperature and washed with 0.1 M cacodylate buffer. Samples with appropriate staining were subsequently stained with 2% buffered osmium tetroxide for 1.5 h followed by 2.5% potassium ferrocyanide for 1.5 h without intermediate washing. The subsequent steps involved washing with water, incubating in 4% pyrogallol for 1 h and additional washes with water. The samples were treated with 2% aqueous osmium tetroxide for 1.5 h followed by rinsing with water. All steps were carried out at room temperature. The next step included incubation in a 1% aqueous uranyl acetate solution at 4°C overnight in the dark. The vials with tissue in 1% uranyl acetate solution were then transferred to a bead bath and incubated at 50°C for 2 h. After washing with water, the samples were treated with filtered 0.66% lead (II) nitrate in 0.03 M aspartic acid with pH adjusted to 5.0 at 50°C for 2 h. Following washes with water, the samples underwent dehydration in an ethanol series followed by propylene oxide. Gradual infiltration with EPON resin (composed of 49% EMbed812, 28% DDSA, 21% NMA and 2% DMP-30) over 4 days at room temperature was performed. The resin infiltrated samples were cured in the oven for 48–72 h at 60°C (Hua et al., 2015).

4.4 | Large volume 3D EM imaging and processing

Approximately 1000–1850 40-nm-thick ultra-thin serial sections were cut with a cross section of either ~1.4 × 0.9 mm or ~0.90 × 0.75 mm, collected on aluminium coated Kapton tape, attached to silicon wafers using double-sided carbon sticky tape and carbon coated (Kasthuri et al., 2015).

Electron microscopy imaging was done using T1 segmented lower in-lens detector on Volumescope 2 scanning electron microscope (Thermo Fisher Scientific) and Maps version 3.22 software for wafer imaging. The images were collected at 10 nm x and y pixels at 1 μs dwell time per pixel. 945 sections were imaged in one and 790 sections were imaged in the second dataset. Individual tiles were montaged to acquire large fields of view. Each dataset was acquired either as 2 × 3 or 3 × 3 tiles with each tile being 8 k × 8 k pixels with 10% overlap between the tiles. The final images were either 15.2 k × 22.4 k or 22.4 × 22.4 k taking into account the 10% overlap. Individual tiles were montaged, normalized for brightness/contrast and linearly aligned using TrakEM2, an *ImageJ* plugin (Cardona et al., 2012). Further nonlinear alignment of the linearly aligned stack was done on Argonne National Laboratory's super computer, Cooley, using the program *aligntk* (https://mmbios.pitt.edu/aligntk-home). Final volumes used for analysis for one mouse was 119 μm × 195 μm × 37.8 μm, and the other mouse was 200 μm × 182 μm × 31.6 μm.

4.5 | Stereotaxic injections for optogenetics and slice physiology

Stereotactic injections of virus were performed as previously described (Carroll et al., 2022; Mo & Sherman, 2019) using a 1-μL Hamilton syringe at postnatal days 24–28. For dual-colour fluorescence imaging experiments, 400 nL of AAV5-EF1a-double floxed-hChR2 (H134R)-mCherry-WPRE-HGHpA (Addgene viral prep no. 20297-AAV5) was injected in S1, while 400 nL of AAV8-Ef1a-Con/Foff 2.0-BFP (Addgene viral prep no. 137130-AAV8) was injected into M1. For optogenetics experiments, 400 nL (50 nL/min injection rate) of AAV5-EF1a-double floxed-hChR2(H134R)-mCherry-WPRE-HGHpA (Addgene viral prep no. 20297-AAV5) was injected into right M1 (−1.3 ML, +1.5 AP, −0.6 DV) or S1 (−3.1 ML, −0.8 AP, −0.5 DV form dura surface) to allow photostimulation of L5 corticostriatal projections in a Cre-dependent fashion. Two weeks were given for expression before recordings were obtained.

4.6 | Acute slice preparation and whole cell recordings

Animals were deeply anesthetized (nonresponsive to toe pinch) and immediately transcardially perfused with 8 mL of ice cold oxygenated (95% O_2, 5%CO_2) artificial cerebrospinal fluid, which contained the following

(in mM): 125 NaCl, 25 $NaHCO_3$, 3 KCl, 1.25 NaH_2PO_4, 1 $MgCl_2$, 2 $CaCl_2$ and 25 glucose. The brain was extracted, glue-mounted on a vibratome platform (Leica) for either standard coronal slices or at a 55° angle from the midline to preserve descending cortical L5 axons (Agmon & Connors, 1991) and sliced in the same solution (also ice-cold). Slices were cut at 350 or 400 μm thickness. Brain slices were then transferred to 33°C oxygenated artificial cerebrospinal fluid that was allowed to return to room temperature thereafter. This recovery in artificial cerebrospinal fluid occurred in the dark for 1 h before recordings began.

Slices containing terminals from M1 or S1 in the CP were visualized using differential interference contrast with a Axioskop 2FS microscope (Carl Zeiss). Fluorescence from ChR2 expression was confirmed using the 5× air objective and guided recording locations. Recordings were made with a Multiclamp 700B amplifier and pCLAMP software (Molecular Devices). Recording glass pipettes with 4–6 MΩ resistance were filled with intracellular solution containing the following (in mM): 117 K-gluconate, 13 KCl, 1 $MgCl_2$, 0.07 $CaCl_2$, 10 Hepes, 0.1 EGTA, 2 Na2-ATP, 0.4 Na-GTP, pH 7.3 and 290 mOsm. Pharmacological inactivation of iGluRs was induced by bath application of 50 μM DNQX and 100 μM AP5.

Optogenetic stimulation was performed as previously (Carroll et al., 2022; Mo & Sherman, 2019). Briefly, stimulation was delivered using a 355 nm laser (DPSS: 3505–100), controlled with galvanometer mirrors (Cambridge Technology) focused on the slice through a 5× air objective using custom software in MATLAB (MathWorks). This approach gives us the capability of focal optogenetic stimulation of ChR2, which is indeed sensitive to a relatively broad light spectrum that includes UV light (Stahlberg et al., 2019). That is, we can activate ChR2+ axons distal from the recording site (Miller-Hansen & Sherman, 2022; Mo et al., 2017; Mo & Sherman, 2019), avoiding the confounds introduced by stimulating synaptic terminals (Jackman et al., 2014; Mo & Sherman, 2019), as occurs in comparable experiments using full field LED stimulation.

To determine synaptic properties, four pulses of 1-ms duration were delivered at 100 ms interstimulus interval (ISI) during recordings. To test for the presence of mGluR responses, high-frequency optogenetic stimulation using 20 pulses of 1-ms duration was delivered at 12 ms ISI (83 Hz), and responses were recorded in current clamp.

4.7 | Data analysis and statistics

All EM data analysis involved the examination of 3D EM serially reconstructed volumes. The datasets were manually annotated using Knossos software (Boergens et al., 2017). The cytoplasmic and mitochondrial labeled terminals were visually identified and differentiated from each other and unlabeled terminals (Sampathkumar et al., 2021a). The Knossos software was used for identification of densely labeled terminal zone and 3D reconstructing the dendritic arbor of neurons in CP. For measuring terminal, spine head and dendrite diameters, we utilized the 3D EM stack and placed a node in the Knossos software that corresponded to the largest diameter by scrolling through the stack. The node radius, obtained in pixels from the software, was later converted into diameter in nanometres. To evaluate the presence of mitochondria, spine apparatus and multiple post-synaptic targets, examiners scrolled through the 3D reconstructed stack and recorded the presence or absence of mitochondria and spine apparatus within the labeled and unlabeled terminals, as well as the number of number of post-synaptic contacts made by the terminals. Statistical analyses involved non-parametric tests (Mann–Whitney U test and χ^2 test) plus correlation coefficient analyses that were performed on data using custom MATLAB software.

Electrophysiological data were collected using custom MATLAB software. The amplitude of responses to stimulation pulses was measured by subtracting the average value for 20 ms before the delivery of a pulse (baseline) from the maximum value of the peak. The paired-pulse ratio (PPR) was calculated by dividing the amplitude of the second pulse by that of the first pulse. Statistical analyses were conducted in GraphPad Prism (v7.0). Image analysis was conducted in FIJI (NIH), and figures were produced using Adobe Illustrator.

4.8 | Data sharing plan

The authors are committed to the appropriate sharing of scientific data in accordance with the NIH Grants Policy on Availability of Research Results: Publications, Intellectual Property Rights and Sharing Biomedical Research Resources. All methods used to create the results of this proposal will be made publicly available in GitHub and available by request from the authors. There is no reason to limit the access or sharing of any of the data that will be generated in this publication. Large datasets will be shared through NIH-designated data repositories (BossDB). We will leverage our storage capabilities at Argonne (> 100 petabytes of storage), and for distribution of large datasets, we will use Globus, which has connection points worldwide and was designed for the transfer of large scientific datasets (globus.org). We have experience using Globus sharing data with multiple collaborators worldwide.

AUTHOR CONTRIBUTIONS

Vandana Sampathkumar, Kevin P. Koster, Briana J. Carroll, and Narayanan Kasthuri were responsible for all phases of the work, including experimental design, data collection, data analysis, and preparation of the manuscript. S. Murray Sherman was responsible for experimental design, data analysis, and preparation of the manuscript.

ACKNOWLEDGEMENTS

We thank Dr. Jotham Austin II, The University of Chicago Advanced Electron Microscopy Core Facility (RRID: SCR_019198). This research used resources of the Argonne Leadership Computing Facility, which is a DOE Office of Science User Facility supported under Contract DE-AC02-06CH11357. This work was supported by NIH Grant Nos. NS094184 and NS113922 and a NSF Neuronex 2014862.

CONFLICT OF INTEREST STATEMENT

The authors have no competing financial interests to divulge.

PEER REVIEW

The peer review history for this article is available at https://www.webofscience.com/api/gateway/wos/peer-review/10.1111/ejn.16538.

DATA AVAILABILITY STATEMENT

All authors will be responsible for overseeing the regular backup of the data from their laboratories. We will comply with the NIH Data Sharing requirement (http://grants.nih.gov/grants/policy/data_sharing). All tools (data, assays, libraries, research tools, reagents, etc.) will be made available, in accordance with the policy. Our practices are

- All datasets made available for sharing in accord with NIH timeliness guidelines "no later than the date of acceptance for publication of the main findings from the final dataset."
- Data will be shared via electronic transfer or shipping of hard drives as required on request.
- Datasets shall consist of electronic copies of raw EM images, all annotations, protocols of injections, sequences for viruses, and so on.
- All code (MATLAB) will be shared on request.

ORCID

Vandana Sampathkumar https://orcid.org/0000-0002-0577-7164

S. Murray Sherman https://orcid.org/0000-0002-1520-2778

REFERENCES

Agmon, A., & Connors, B. W. (1991). Thalamocortical responses of mouse somatosensory (barrel) cortex in vitro. *Neuroscience*, *41*, 365–379. https://doi.org/10.1016/0306-4522(91)90333-J

Alloway, K. D., Lou, L., Nwabueze-Ogbo, F., & Chakrabarti, S. (2006). Topography of cortical projections to the dorsolateral neostriatum in rats: Multiple overlapping sensorimotor pathways. *The Journal of Comparative Neurology*, *499*, 33–48. https://doi.org/10.1002/cne.21039

Boergens, K. M., Berning, M., Bocklisch, T., Bräunlein, D., Drawitsch, F., Frohnhofen, J., Herold, T., Otto, P., Rzepka, N., Werkmeister, T., Werner, D., Wiese, G., Wissler, H., & Helmstaedter, M. (2017). webKnossos: Efficient online 3D data annotation for connectomics. *Nature Methods*, *14*(7), 691–694. https://doi.org/10.1038/nmeth.4331

Borczyk, M., Śliwińska, M. A., Caly, A., Bernas, T., & Radwanska, K. (2019). Neuronal plasticity affects correlation between the size of dendritic spine and its postsynaptic density. *Scientific Reports*, *9*, 1693. https://doi.org/10.1038/s41598-018-38412-7

Cardona, A., Saalfeld, S., Schindelin, J., Arganda-Carreras, I., Preibisch, S., Longair, M., Tomancak, P., Hartenstein, V., & Douglas, R. J. (2012). TrakEM2 software for neural circuit reconstruction. *PLoS ONE*, *7*(6), e38011. https://doi.org/10.1371/journal.pone.0038011

Carroll, B. J., Sampathkumar, V., Kasthuri, N., & Sherman, S. M. (2022). Layer 5 of cortex innervates the thalamic reticular nucleus in mice. *Proceedings of the National Academy of Sciences of the United States of America*, *119*, e2205209119. https://doi.org/10.1073/pnas.2205209119

Charpier, S., Pidoux, M., & Mahon, S. (2020). Converging sensory and motor cortical inputs onto the same striatal neurons: An in vivo intracellular investigation. *PLoS ONE*, *15*, e0228260. https://doi.org/10.1371/journal.pone.0228260

Cserép, C., Pósfai, B., Schwarcz, A. D., & Dénes, Á. (2018). Mitochondrial ultrastructure is coupled to synaptic performance at axonal release sites. *Eneuro*, *5*(1). https://doi.org/10.1523/ENEURO.0390-17.2018

Deller, T., Korte, M., Chabanis, S., Drakew, A., Schwegler, H., Stefani, G. G., Zuniga, A., Schwarz, K., Bonhoeffer, T., Zeller, R., Frotscher, M., & Mundel, P. (2003). Synaptopodin-deficient mice lack a spine apparatus and show deficits in synaptic plasticity. *Proceedings of the National Academy of Sciences of the United States of America*, *100*(18), 10494–10499. https://doi.org/10.1073/pnas.1832384100

Freund, T. F., Powell, J. F., & Smith, A. D. (1984). Tyrosine hydroxylase-immunoreactive boutons in synaptic contact with identified striatonigral neurons, with particular reference to dendritic spines. *Neuroscience*, *13*, 1189–1215. https://doi.org/10.1016/0306-4522(84)90294-X

Gerfen, C. R., Paletzki, R., & Heintz, N. (2013). GENSAT BAC cre-recombinase driver lines to study the functional organization of cerebral cortical and basal ganglia circuits. *Neuron*, *80*(6), 1368–1383. https://doi.org/10.1016/j.neuron.2013.10.016

Harris, J. A., Hirokawa, K. E., Sorensen, S. A., Gu, H., Mills, M., Ng, L. L., Bohn, P., Mortrud, M., Ouellette, B., Kidney, J., Smith, K. A., Dang, C., Sunkin, S., Bernard, A., Oh, S. W., Madisen, L., & Zeng, H. (2014). Anatomical characterization of Cre driver mice for neural circuit mapping and

manipulation. *Frontiers in Neural Circuits*, *8*, 76. https://doi.org/10.3389/fncir.2014.00076

Hintiryan, H., Foster, N. N., Bowman, I., Bay, M., Song, M. Y., Gou, L., Yamashita, S., Bienkowski, M. S., Zingg, B., Zhu, M., Yang, X. W., Shih, J. C., Toga, A. W., & Dong, H. W. (2016). The mouse cortico-striatal projectome. *Nature Neuroscience*, *19*, 1100–1114. https://doi.org/10.1038/nn.4332

Hoffer, Z. S., & Alloway, K. D. (2001). Organization of corticostriatal projections from the vibrissal representations in the primary motor and somatosensory cortical areas of rodents. *The Journal of Comparative Neurology*, *439*, 87–103. https://doi.org/10.1002/cne.1337

Holler, S., Köstinger, G., Martin, K. A. C., Schuhknecht, G. F. P., & Stratford, K. J. (2021). Structure and function of a neocortical synapse. *Nature*, *591*, 111–116. https://doi.org/10.1038/s41586-020-03134-2

Hooks, B. M., Papale, A. E., Paletzki, R. F., Feroze, M. W., Eastwood, B. S., Couey, J. J., Winnubst, J., Chandrashekar, J., & Gerfen, C. R. (2018). Topographic precision in sensory and motor corticostriatal projections varies across cell type and cortical area. *Nature Communications*, *9*, 3549. https://doi.org/10.1038/s41467-018-05780-7

Hua, Y., Laserstein, P., & Helmstaedter, M. (2015). Large-volume en-bloc staining for electron microscopy-based connectomics. *Nature Communications*, *6*, 7923. https://doi.org/10.1038/ncomms8923

Hunnicutt, B. J., Long, B. R., Kusefoglu, D., Gertz, K. J., Zhong, H., & Mao, T. (2014). A comprehensive thalamocortical projection map at the mesoscopic level. *Nature Neuroscience*, *17*, 1276–1285. https://doi.org/10.1038/nn.3780

Ingham, C. A., Hood, S. H., Taggart, P., & Arbuthnott, G. W. (1998). Plasticity of synapses in the rat neostriatum after unilateral lesion of the nigrostriatal dopaminergic pathway. *The Journal of Neuroscience*, *18*, 4732–4743. https://doi.org/10.1523/JNEUROSCI.18-12-04732.1998

Jackman, S. L., Beneduce, B. M., Drew, I. R., & Regehr, W. G. (2014). Achieving high-frequency optical control of synaptic transmission. *The Journal of Neuroscience*, *34*, 7704–7714. https://doi.org/10.1523/JNEUROSCI.4694-13.2014

Johansson, Y., & Silberberg, G. (2020). The functional organization of cortical and thalamic inputs onto five types of striatal neurons is determined by source and target cell identities. *Cell Reports*, *30*, 1178–1194. https://doi.org/10.1016/j.celrep.2019.12.095

Jones, E. G. (2007). *The thalamus* (Second ed.). Cambridge University Press.

Jones, E. G., & Powell, T. P. (1969). Morphological variations in the dendritic spines of the neocortex. *Journal of Cell Science*, *5*, 509–529. https://doi.org/10.1242/jcs.5.2.509

Kaiser, T., Ting, J. T., Monteiro, P., & Feng, G. (2016). Transgenic labeling of parvalbumin-expressing neurons with tdTomato. *Neuroscience*, *321*, 236–245. https://doi.org/10.1016/j.neuroscience.2015.08.036

Kasthuri, N., Hayworth, K. J., Berger, D. R., Schalek, R. L., Conchello, J. A., Knowles-Barley, S., Lee, D., Vazquez-Reina, A., Kaynig, V., Jones, T. R., Roberts, M., Morgan, J. L., Tapia, J. C., Seung, H. S., Roncal, W. G., Vogelstein, J. T., Burns, R., Sussman, D. L., Priebe, C. E., … Lichtman, J. W. (2015). Saturated reconstruction of a volume of neocortex. *Cell*, *162*, 648–661. https://doi.org/10.1016/j.cell.2015.06.054

Kemp, J. M., & Powell, T. P. (1971). The connexions of the striatum and globus pallidus: Synthesis and speculation. Philosophical transactions of the Royal Society of London. *Series B Biological Sciences*, *262*, 441–457. https://doi.org/10.1098/rstb.1971.0106

Kreitzer, A. C. (2009). Physiology and pharmacology of striatal neurons. *Annual Review of Neuroscience*, *32*, 127–147. https://doi.org/10.1146/annurev.neuro.051508.135422

Lam, S. S., Martell, J. D., Kamer, K. J., Deerinck, T. J., Ellisman, M. H., Mootha, V. K., & Ting, A. Y. (2015). Directed evolution of APEX2 for electron microscopy and proximity labeling. *Nature Methods*, *12*, 51–54. https://doi.org/10.1038/nmeth.3179

Lanciego, J. L., Luquin, N., & Obeso, J. A. (2012). Functional neuroanatomy of the basal ganglia. *Cold Spring Harbor Perspectives in Medicine*, *2*, a009621. https://doi.org/10.1101/cshperspect.a009621

Lee, C. R., Yonk, A. J., Wiskerke, J., Paradiso, K. G., Tepper, J. M., & Margolis, D. J. (2019). Opposing influence of sensory and motor cortical input on striatal circuitry and choice behavior. *Current Biology*, *29*, 1313–1323. https://doi.org/10.1016/j.cub.2019.03.028

Lee, K. J., Park, I. S., Kim, H., Greenough, W. T., Pak, D. T., & Rhyu, I. J. (2013). Motor skill training induces coordinated strengthening and weakening between neighboring synapses. *The Journal of Neuroscience*, *33*, 9794–9799. https://doi.org/10.1523/JNEUROSCI.0848-12.2013

Martell, J. D., Deerinck, T. J., Lam, S. S., Ellisman, M. H., & Ting, A. Y. (2017). Electron microscopy using the genetically encoded APEX2 tag in cultured mammalian cells. *Nature Protocols*, *12*(9), 1792–1816. https://doi.org/10.1038/nprot.2017.065

Meyer, D., Bonhoeffer, T., & Scheuss, V. (2014). Balance and stability of synaptic structures during synaptic plasticity. *Neuron*, *82*, 430–443. https://doi.org/10.1016/j.neuron.2014.02.031

Miller-Hansen, A. J., & Sherman, S. M. (2022). Conserved patterns of functional organization between cortex and thalamus in mice. *Proceedings of the National Academy of Sciences of the United States of America*, *119*, e2201481119. https://doi.org/10.1073/pnas.2201481119

Mo, C., Petrof, I., Viaene, A. N., & Sherman, S. M. (2017). Synaptic properties of the lemniscal and paralemniscal pathways to the mouse somatosensory thalamus. *Proceedings of the National Academy of Sciences of the United States of America*, *114*, E6212–E6221. https://doi.org/10.1073/pnas.1703222114

Mo, C., & Sherman, S. M. (2019). A sensorimotor pathway via higher-order thalamus. *The Journal of Neuroscience*, *39*, 692–704. https://doi.org/10.1523/JNEUROSCI.1467-18.2018

Morgenstern, N. A., Isidro, A. F., Israely, I., & Costa, R. M. (2022). Pyramidal tract neurons drive amplification of excitatory inputs to striatum through cholinergic interneurons. *Science Advances*, *8*, eabh4315. https://doi.org/10.1126/sciadv.abh4315

Nauta, H. J., Pritz, M. B., & Lasek, R. J. (1974). Afferents to the rat caudoputamen studied with horseradish peroxidase. An evaluation of a retrograde neuroanatomical research method. *Brain Research*, *67*, 219–238. https://doi.org/10.1016/0006-8993(74)90274-1

Oh, S. W., Harris, J. A., Ng, L., Winslow, B., Cain, N., Mihalas, S., Wang, Q., Lau, C., Kuan, L., Henry, A. M., Mortrud, M. T., Ouellette, B., Nguyen, T. N., Sorensen, S. A., Slaughterbeck, C. R., Wakeman, W., Li, Y., Feng, D., Ho, A., ... Zeng, H. (2014). A mesoscale connectome of the mouse brain. *Nature*, *508*, 207–214. https://doi.org/10.1038/nature13186

Paxinos, G., & Franklin, K. B. J. (2008). *The mouse brain in stereotaxic coordinates*. Academic Press.

Prasad, J. A., Carroll, B. J., & Sherman, S. M. (2020). Layer 5 corticofugal projections from diverse cortical areas: Variations on a pattern of thalamic and extra-thalamic targets. *Journal of Neuroscience*, *40*, 5785–5796. https://doi.org/10.1523/JNEUROSCI.0529-20.2020

Ramanathan, S., Hanley, J. J., Deniau, J. M., & Bolam, J. P. (2002). Synaptic convergence of motor and somatosensory cortical afferents onto GABAergic interneurons in the rat striatum. *The Journal of Neuroscience*, *22*, 8158–8169. https://doi.org/10.1523/JNEUROSCI.22-18-08158.2002

Sampathkumar, V., Miller-Hansen, A., Sherman, S. M., & Kasthuri, N. (2021a). Integration of signals from different cortical areas in higher order thalamic neurons. *Proceedings of the National Academy of Sciences of the United States of America*, *118*. https://doi.org/10.1073/pnas.2104137118

Sampathkumar, V., Miller-Hansen, A., Sherman, S. M., & Kasthuri, N. (2021b). An ultrastructural connectomic analysis of a higher order thalamocortical circuit in the mouse. *European Journal of Neuroscience*, *53*, 750–762. https://doi.org/10.1111/ejn.15092

Sherman, S. M., & Guillery, R. W. (1998). On the actions that one nerve cell can have on another: Distinguishing "drivers" from "modulators". *Proceedings of the National Academy of Sciences of the United States of America*, *95*, 7121–7126. https://doi.org/10.1073/pnas.95.12.7121

Sherman, S. M., & Guillery, R. W. (2013). *Functional connections of cortical areas: A new view from the thalamus*. MIT Press. https://doi.org/10.7551/mitpress/9780262019309.001.0001

Smith, J. B., Chakrabarti, S., Mowery, T. M., & Alloway, K. D. (2022). Convergence of forepaw somatosensory and motor cortical projections in the striatum, claustrum, thalamus, and pontine nuclei of cats. *Brain Structure & Function*, *227*, 361–379. https://doi.org/10.1007/s00429-021-02405-6

Spacek, J. (1985). Three-dimensional analysis of dendritic spines. II. Spine apparatus and other cytoplasmic components. *Anatomy and Embryology (Berlin)*, *171*(2), 235–243. https://doi.org/10.1007/BF00341418

Stahlberg, M. A., Ramakrishnan, C., Willig, K. I., Boyden, E. S., Deisseroth, K., & Dean, C. (2019). Investigating the feasibility of channelrhodopsin variants for nanoscale optogenetics. *Neurophotonics*, *6*, 015007. https://doi.org/10.1117/1.NPh.6.1.015007

Tepper, J. M., Koós, T., Ibanez-Sandoval, O., Tecuapetla, F., Faust, T. W., & Assous, M. (2018). Heterogeneity and diversity of striatal GABAergic interneurons: Update 2018. *Frontiers in Neuroanatomy*, *12*, 91. https://doi.org/10.3389/fnana.2018.00091

Toni, N., Buchs, P.-A., Nikonenko, I., Bron, C. R., & Muller, D. (1999). LTP promotes formation of multiple spine synapses between a single axon terminal and a dendrite. *Nature*, *402*, 421–425. https://doi.org/10.1038/46574

Usrey, W. M., & Sherman, S. M. (2019). Corticofugal circuits: Communication lines from the cortex to the rest of the brain. *The Journal of Comparative Neurology*, *527*, 640–650. https://doi.org/10.1002/cne.24423

Usrey, W. M., & Sherman, S. M. (2021). *Exploring thalamocortical interactions: Circuitry for sensation, action, and cognition*. Oxford University Press.

Van Horn, S. C., Erisir, A., & Sherman, S. M. (2000). Relative distribution of synapses in the A-laminae of the lateral geniculate nucleus of the cat. *The Journal of Comparative Neurology*, *416*, 509–520. https://doi.org/10.1002/(SICI)1096-9861(20000124)416:4<509::AID-CNE7>3.0.CO;2-H

Wilson, C. J. (2013). Active decorrelation in the basal ganglia. *Neuroscience*, *250*, 467–482. https://doi.org/10.1016/j.neuroscience.2013.07.032

Wilson, C. J., Groves, P. M., Kitai, S. T., & Linder, J. C. (1983). Three-dimensional structure of dendritic spines in the rat neostriatum. *The Journal of Neuroscience*, *3*, 383–388. https://doi.org/10.1523/JNEUROSCI.03-02-00383.1983

Wilson, J. W. (2004). Basal Ganglia. In G. M. Shepherd (Ed.), *Synaptic organization of the brain* (pp. 361–414). Oxford University Press. https://doi.org/10.1093/acprof:oso/9780195159561.003.0009

How to cite this article: Sampathkumar, V., Koster, K. P., Carroll, B. J., Sherman, S. M., & Kasthuri, N. (2024). Synaptic integration of somatosensory and motor cortical inputs onto spiny projection neurons of mice caudoputamen. *European Journal of Neuroscience*, 1–16. https://doi.org/10.1111/ejn.16538